

LETTER TO THE EDITOR

Evidence for extended [CII] and dust emission in local dwarf galaxies

M. Romano^{*1,2}, D. Donevski^{1,3,4}, Junais¹, A. Nanni^{1,5}, M. Ginolfi⁶, G. C. Jones⁷, I. Shivaei⁸, G. Lorenzon¹, M. Hamed¹, D. Salak^{9,10}, and P. Sawant¹

¹ National Centre for Nuclear Research, ul. Pasteura 7, 02-093 Warsaw, Poland

² INAF - Osservatorio Astronomico di Padova, Vicolo dell'Osservatorio 5, I-35122, Padova, Italy

³ SISSA, Via Bonomea 265, Trieste, Italy

⁴ IFPU - Institute for fundamental physics of the Universe, Via Beirut 2, 34014 Trieste, Italy

⁵ INAF - Osservatorio astronomico d'Abruzzo, Via Maggini SNC, 64100, Teramo, Italy

⁶ Dipartimento di Fisica e Astronomia, Università di Firenze, Via G. Sansone 1, 50019, Sesto Fiorentino (Firenze), Italy

⁷ Department of Physics, University of Oxford, Denys Wilkinson Building, Keble Road, Oxford OX1 3RH, UK

⁸ Centro de Astrobiología (CAB), CSIC-INTA, Ctra. de Ajalvir km 4, Torrejón de Ardoz, E-28850, Madrid, Spain

⁹ Institute for the Advancement of Higher Education, Hokkaido University, Kita 17 Nishi 8, Kita-ku, Sapporo, Hokkaido 060-0817, Japan

¹⁰ Department of Cosmosciences, Graduate School of Science, Hokkaido University, Kita 10 Nishi 8, Kita-ku, Sapporo, Hokkaido 060-0810, Japan

February 28, 2024

ABSTRACT

Aims. The evolution of dwarf galaxies is dramatically affected by gaseous and dusty outflows, as they can easily deprive their interstellar medium of the material needed for the formation of new stars, simultaneously enriching their surrounding circumgalactic medium (CGM). In this Letter, we present the first evidence for extended [CII] 158 μm line and dust continuum emission in local dwarf galaxies hosting star-formation-driven outflows.

Methods. By stacking the [CII], far-infrared and near-UV (NUV) emission obtained from *Herschel* and GALEX data, we derive the average radial profiles, and compare the spatial extension of gas, dust, and stellar activity in dwarf galaxies.

Results. We find that [CII] and dust emissions are comparable to each other, and more extended than the NUV continuum. The [CII] size is in agreement with that measured for $z > 4$ star-forming galaxies, suggesting that similar mechanisms could be at the origin of the observed atomic carbon reservoir around local and high- z sources. The cold dust follows the [CII] emission, going beyond the stellar continuum as opposed to what is typically observed in the early Universe where measurements can be affected by the poor sensitivity and faintness of dust emission in the CGM of high- z galaxies.

Conclusions. We attribute the extended [CII] and dust continuum emission to the presence of galactic outflows. As local dwarf galaxies are considered analogs of primordial sources, we could expect that comparable feedback processes can be at the origin of the observed [CII] halos at $z > 4$, dominating over other possible formation mechanisms.

Key words. Galaxies: dwarf - Galaxies: evolution - Galaxies: ISM - Galaxies: starburst - ISM: jets and outflows

1. Introduction

The evolution of galaxies is regulated by the tangled interplay between gas, stars, and dust in their interstellar medium (ISM). This picture is further complicated by a continuous exchange of material with the surrounding circumgalactic medium (CGM) that can be driven by merging activity, inflow, and outflow of gas, giving rise to the so-called baryon cycle (see e.g., Tumlinson et al. 2017; Péroux & Howk 2020 for a review). Typically, the CGM can extend up to several kiloparsec, hosting a large reservoir of cosmic web-accreted gas and/or processed material ejected from galaxies, that can be used as fuel for future star formation.

Gas can be expelled from the ISM and injected into the CGM (or even further into the intergalactic medium, IGM) through high-velocity winds produced by stellar feedback (e.g., Gallerani et al. 2018; Ginolfi et al. 2020b; Romano et al. 2023) and ac-

tive galactic nuclei (AGNs, e.g., Cicone et al. 2015; Rupke et al. 2017; Jones et al. 2023). The ejected material can be made of dust, and ionized, atomic, and molecular gas that can be explored with different tracers and methods, including indirect observations of UV absorption lines along quasars lines of sight (e.g., Werk et al. 2016; Guo et al. 2020), or direct detections of emission lines such as HI 21 cm, Ly α , [CII] 158 μm , or CO transitions (e.g., Fujimoto et al. 2020; Sanderson et al. 2021; Ianjamasimanana et al. 2022; Jones et al. 2023).

Particularly, the [CII] line has gained a prominent role in the field of galaxy evolution, as it is a major coolant of the ISM and can provide precious information on the gas kinematics and morphology, star-formation activity, stellar feedback, and CGM enrichment (e.g., Ginolfi et al. 2020a; Jones et al. 2021; Romano et al. 2021). Due to its low ionization potential (i.e., 11.3 eV, as compared to the 13.6 eV of neutral hydrogen), [CII] can trace different gas phases (e.g., Pineda et al. 2013; Zanella et al. 2018; Heintz et al. 2021), although many studies suggest that

* E-mail: michael.romano@ncbj.gov.pl

the bulk of its emission originates from the cold, neutral gas (e.g., Díaz-Santos et al. 2017; Cormier et al. 2019). Recently, ALMA observations have revealed the existence of diffuse [CII] components (sometimes referred as “[CII] halos”) around $z > 4$ galaxies, that result to be more extended than the underlying dust and stellar emission traced by the rest-frame UV and far-infrared (FIR) continuum (e.g., Fujimoto et al. 2019, 2020; Ginolfi et al. 2020a; Herrera-Camus et al. 2021; Akins et al. 2022; Fudamoto et al. 2022; Lambert et al. 2023; Mitsunashi et al. 2023). Such a wide gas distribution can be ascribed to different scenarios (e.g., satellites around the central galaxy, cold gas streams; Fujimoto et al. 2019), although it is often linked to the presence of star-formation-driven winds that can drag the gas outside of the galaxies enriching the surrounding CGM (e.g., Hopkins et al. 2012; Ginolfi et al. 2020b; Pizzati et al. 2020; Herrera-Camus et al. 2021). On the other hand, the spatial distribution of [CII], as compared to the UV and FIR emission, has been poorly investigated in the local Universe, with only a few individual sources showing hints for extended [CII] emission (e.g., Madden et al. 1993; Veilleux et al. 2021).

In this Letter, we report the first evidence for extended [CII] and dust emission around nearby dwarf galaxies. We use the sample of dwarf sources in Romano et al. (2023), in which we found signatures of atomic¹ outflowing gas through *Herschel*/PACS [CII] observations. In that work, we found clues for outflow-induced CGM enrichment, and for extended [CII] emission as compared to the UV continuum. This motivated us to undertake a more in-depth investigation of the spatial distribution of [CII] in those galaxies, along with its origin and link to [CII] halos in more distant sources.

The sample of dwarf galaxies is described in Sect. 2. Section 3 reports the method used to stack the UV, FIR, and [CII] emission of the galaxies, and to retrieve the corresponding radial profiles. We present and discuss our results in Sect. 4, and finally provide our conclusions in Sect. 5. We adopt a Λ -CDM cosmology with $H_0 = 70 \text{ km s}^{-1} \text{ Mpc}^{-1}$, $\Omega_m = 0.3$, and $\Omega_\Lambda = 0.7$. At the mean redshift of the sample (i.e., $z_{\text{mean}} = 0.012$), 1 arcsecond corresponds to 0.2 kpc.

2. Sample and observations

We analyzed the sample of 29 dwarf sources in Romano et al. (2023). Those targets were drawn from the Dwarf Galaxy Survey (DGS; Madden et al. 2013, 2014) that observed a collection of 48 low-metallicity ($7.14 < 12 + \log(\text{O}/\text{H}) < 8.43$) local dwarf galaxies (at distances $< 200 \text{ Mpc}$) in the FIR with the PACS (Poglitsch et al. 2010) and SPIRE (Griffin et al. 2010) instruments mounted on the *Herschel* Space Observatory. All the galaxies benefit from a wide photometric coverage, going from the UV to the sub-mm (Madden et al. 2013). Of particular relevance for this work are the observed UV and FIR continuum emissions. Indeed, we used the near-UV (NUV; $\lambda_{\text{eff}} \sim 2271 \text{ \AA}$) and $160 \mu\text{m}$ emission detected by the Galaxy Evolution Explorer (GALEX; Martin et al. 2005) and *Herschel* telescopes as proxies for recent star formation from young stars and dust continuum, respectively, with the goal of a final comparison with the gas distribution traced by the [CII] line. In Romano et al. (2023), we modeled the spectral energy distributions of the DGS sources and took advantage of their spectroscopic information to retrieve physical parameters, including stellar masses ($\log(M_*/M_\odot) \sim 5 - 10$) and star-formation rates

¹ In Romano et al. (2023), we indeed assume that $\sim 70\%$ of the [CII] emission originates from the atomic phase (e.g., Cormier et al. 2019).

(SFR $\sim 0.001 - 10 M_\odot \text{ yr}^{-1}$). We found that most of the galaxies with the largest SFRs show clear signatures of outflowing gas as traced by broad emissions in the high-velocity tails of their [CII] spectra, with the remaining sources likely affected by weaker winds detected in their stacked profile.

3. Method

When comparing the average spatial distribution of the *Herschel* [CII] and dust continuum with the NUV continuum from GALEX, we want to be sensitive to the presence of faint and possibly diffuse emission in the outskirts of our galaxies. Because of this, we performed a stacking of their intensity maps. In the following, we briefly describe the stacking procedure for each tracer, as well as their radial profile extractions.

3.1. [CII] stacking

We started from the [CII] intensity maps of the 29 dwarf galaxies of our sample, obtained by summing the spectral channels covering the emission line in the continuum-subtracted PACS data cubes (Romano et al. 2023). We run the CASA (Common Astronomy Software Applications package; McMullin et al. 2007) task IMFIT to fit a 2D Gaussian function to each map and obtain an initial guess on the corresponding target properties, i.e., peak coordinates, full width at half maximum (FWHM) of the major and minor axis. Because of their noisy intensity maps, the fit did not converge for three sources that we thus excluded from our analysis. In order not to contaminate the final average [CII] profile of the sample, we further removed three systems that were classified as mergers in Romano et al. (2023), and seven objects with visually-disturbed morphology or with the peak of emission shifted towards the edge of the PACS field of view (that would artificially modify the average emission at the largest spatial scales of our interest). We spatially aligned the remaining 16 galaxies based on their best-fit coordinates, and stacked them through the following equation:

$$S_{\text{stack}} = \frac{\sum_{i=1}^N S_i \cdot w_i}{\sum_{i=1}^N w_i}, \quad (1)$$

where S_i is the flux of the generic spatial pixel for the i -th galaxy, N is the number of stacked sources, and $w_i = 1/\sigma_i^2$ is the weighting factor, with σ_i the spatial rms associated to each image. As the size of the spatial pixels for each galaxy can be different, we degraded them to the worst spatial resolution among the entire sample (i.e., $3''$) by resampling the images before stacking.

3.2. FIR stacking

To measure the spatial extent of the dust continuum in our galaxies, we took advantage of the *Herschel*/PACS maps at $160 \mu\text{m}$. Observations are available for all but two sources, while no significant emission is detected for 12 galaxies at the position of their optical counterparts. Excluding the latter sources and those flagged as mergers or having disturbed morphology, we ended up with ten galaxies. We made use of the Source Extractor and Photometry tool SEP (Bertin & Arnouts 1996; Barbary 2016) to estimate and subtract the background from the images, as well as to detect the presence of objects in the vicinity of the central targets. We then exploited the source parameters retrieved from SEP (i.e. coordinates, major and minor FWHM, position angle of the modeled ellipse, and peak flux) as first guess to model and subtract those sources with the PetroFit package (Geda et al. 2022)

to avoid altering the emission profile estimates, and stacked the resulting images through Eq. 1.

3.3. UV stacking

We compared the dust distribution with the UV emission from young stars by means of NUV GALEX maps, available for all but five galaxies in our sample. After a first visual inspection of the images, we excluded ten sources with complex morphology (including the three mergers from Romano et al. 2023) that could hamper the comparison with [CII] and FIR profiles, ending up with 14 galaxies. In case of multiple detections of the same source, we co-added the images by taking into account the exposure map of each observation. As done in Sect. 3.2, we then subtracted the background from each image and removed all the spurious objects in the field of view, before stacking all the galaxies with Eq. 1. Since the FWHM of GALEX NUV point-spread function (PSF) is $\sim 5''$, we degraded the resolution of the UV-stacked image to match the one from [CII] and FIR *Herschel* observations (FWHM $\sim 12''$). To do that, we convolved the GALEX image with a 2D Gaussian kernel with $\sigma_{\text{match}} = \sqrt{\sigma_{\text{FIR,PSF}}^2 - \sigma_{\text{UV,PSF}}^2}$, where $\sigma_{\text{FIR,PSF}}$ and $\sigma_{\text{UV,PSF}}$ are obtained by dividing the FIR and UV PSF FWHM by a factor 2.355, respectively.

More information on the galaxies used for the [CII], FIR, and UV stacking and their properties can be found in Appendix A.

3.4. Extraction of the radial profiles

For each stacked image, we extracted the corresponding circularized radial profile. We centered on the brightest pixel in the image, and built concentric annular apertures of 1 pixel width. We estimated the mean value for each aperture, dividing it by its area. The uncertainties are obtained by taking into account the total error on each pixel estimated from the background rms noise image, computed through the Photutils package (Bradley et al. 2023). For a better comparison, we normalized both the mean values and the errors to the maximum of the corresponding radial profile. The results of this procedure are shown in Fig. 1, along with the intensity maps of the stacked images. Since the maps are characterized by different sensitivities, we cut the profiles at the radius at which the uncertainties drop below the corresponding Poissonian² noise (see e.g., Ginolfi et al. 2020b).

4. Results and discussion

4.1. Comparison of the radial profiles

We show in Fig. 1 the radial profiles for the NUV, [CII], and FIR stacked emissions for our dwarf galaxies. The PSF-convolved NUV emission results to be more centrally concentrated than the [CII] and FIR ones, with their spatial extension reaching up to 25 and 30 arcsec from the center, respectively (i.e., 6 to 7 kpc at the mean redshift of the samples, $z_{\text{mean}} = 0.012$).

To provide a quantitative characterization of the spatial distribution of the gas, dust, and star formation in our galaxies, we modeled the light profiles with a Sérsic function (Sérsic 1963), without making any a priori assumption on the Sérsic index. We estimated effective radii $r_{\text{e,UV}} \sim 1.8$ kpc, and $r_{\text{e,FIR}} = r_{\text{e,[CII]}} \sim 2.2$ kpc, and Sérsic index $n \sim 0.5 - 0.6$, close to Gaussian profiles. Although the bulk of the intensity for each tracer is well

² We estimated the Poissonian noise by dividing the rms of the image by the square root of the number of pixels in each annulus.

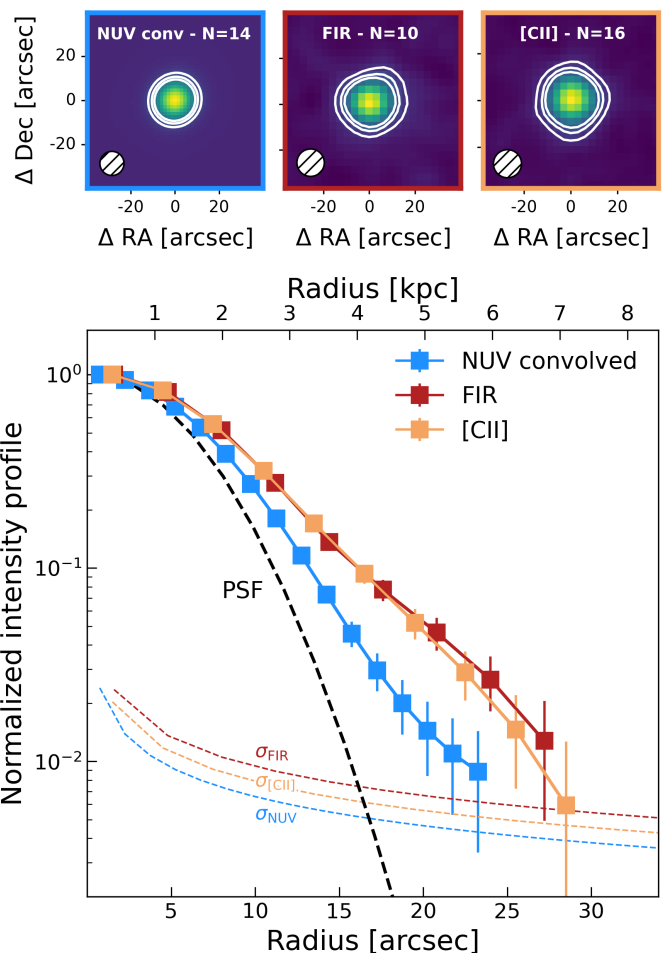


Fig. 1. *Top panels:* Stacked intensity maps of the convolved NUV emission, FIR continuum, and [CII] line (from left to right). In each map, we report the number of stacked sources, and the PSF beam. Contours show the 3, 5, and 7 σ emission. *Bottom panel:* Normalized intensity profiles for the [CII] line (orange), FIR dust continuum (red), and convolved NUV continuum emission (lightblue). The values are obtained in concentric bins of 1 pixel width centered on the peak of the emission. Error bars are computed from noise maps. The FIR PSF is displayed as a dashed black line. Each profile is shown up to the radius at which the uncertainties reach the corresponding Poissonian noise (colored dashed lines). Distance from the center is shown in arcseconds (bottom axis) and kiloparsec at the mean redshift of the sample (top axis).

reproduced, the fits are not able to fully recover the emission at the largest radii. Therefore, we adopted a double Sérsic function, finding a much better agreement with the data than the previous single component (see Appendix B for more details). In this way, each profile is described by a central and an extended component, with the latter being less significant (in terms of total flux) for the UV emission, as opposed to [CII] and FIR continuum. We estimate the effective radius from the combined components in the three profiles as

$$r_{\text{e,comb}} = \sqrt{f_{\text{centr}} r_{\text{e,centr}}^2 + f_{\text{ext}} r_{\text{e,ext}}^2}, \quad (2)$$

where $r_{\text{e,centr}}$ and $r_{\text{e,ext}}$ are the effective radii of the central and extended component, and f_{centr} and f_{ext} represent the fraction of the total flux assigned to each component by the fit, respectively. We obtained $r_{\text{e,UV}} \sim 1.9$ kpc, and $r_{\text{e,FIR}} = r_{\text{e,[CII]}} \sim 2.4$ kpc. Uncertainties on the radii were estimated by performing

Table 1. Estimates of effective radii in kpc of the UV, FIR, and [CII] emission by assuming a single and double Sérsic profile.

	Single Sérsic	Double Sérsic		
		central	extended	combined
$r_{e,UV}$ [kpc]	1.80 ± 0.02	1.68 ± 0.02 (90%)	3.61 ± 0.19 (10%)	1.94 ± 0.03 (100%)
$r_{e,FIR}$ [kpc]	2.22 ± 0.05	1.75 ± 0.18 (76%)	3.65 ± 0.60 (24%)	2.36 ± 0.26 (100%)
$r_{e,[CII]}$ [kpc]	2.22 ± 0.07	1.65 ± 0.15 (62%)	3.12 ± 0.36 (38%)	2.32 ± 0.14 (100%)

Notes. The value reported in parenthesis for the different components of the double Sérsic profile represents the percentage of light attributed to each component during the fit (i.e., f_{centr} and f_{ext} for the central and extended components, and their sum for the combined ones.)

a delete- d jackknife resampling (Shao & Wu 1989), consisting of 100 stacking realizations while removing each time 20% of the sources in the corresponding sample. For all the stacked images, we performed again the radial profiles extraction, taking the standard deviation of the resulting distributions as error. No significant differences were found between the average values of the distributions and those obtained through Eq. 2, suggesting that our analysis is not affected by the presence of possible outliers in the samples. The above results are reported in Table 1.

4.2. Comparison with previous works

In the past years, many works have found that $r_{e,[CII]} > r_{e,UV}$ is a widespread condition in high- z star-forming galaxies (SFGs). For instance, Fujimoto et al. (2020) analyzed the physical extent of [CII] emission in a sample of $z \sim 5$ SFGs drawn from the ALPINE survey (Béthermin et al. 2020; Faisst et al. 2020; Le Fèvre et al. 2020). They found that the ratio between [CII] and UV sizes typically ranges from ~ 2 to 3 with a possible increase with the stellar mass, and that $\sim 30\%$ of the sample presents extended [CII] halos up to radii of 10 kpc. They claimed that star-formation-driven outflows are most likely at the origin of such halos (see also Sect. 4.3). Fudamoto et al. (2022) extended a similar work to $z \sim 7$ sources by stacking their [CII] emission from the REBELS survey (Bouwens et al. 2022). They obtained $r_{e,[CII]}/r_{e,UV} \gtrsim 2$, in agreement with previous results at lower redshift, and suggesting a lack of evolution of the [CII] sizes of SFGs across and beyond the reionization epoch. As for Fujimoto et al. (2020), they also attributed the existence of extended [CII] emission to galactic outflows. Herrera-Camus et al. (2021) obtained the first evidence for star-formation-driven outflow in an individual $z \sim 5$ SFG through dedicated high-resolution [CII] and dust continuum ALMA observations. They found evidence for extended [CII] emission in the source, although with $r_{e,[CII]}/r_{e,UV} = 1.2$, lower than previous estimations for galaxies at similar redshift. Still, they claimed the presence of a [CII] halo likely produced by the feedback activity in the galaxy. Finally, Lambert et al. (2023) have recently found a strong evidence for diffuse [CII] emission in a $z \sim 5.3$ SFG, that is twice more extended than the rest-frame UV size. In this case, they suggest a merging event at the origin of the observed extended [CII] emission, with no significant evidence for outflows (although deeper or higher signal-to-noise observations might be necessary for outflow identification).

We show in Fig. 2 (upper panel) the comparison between $r_{e,[CII]}$ and $r_{e,UV}$ for these high- z galaxies³, and for our local

³ For ALPINE, we show only the sources with reliable size measurements for both [CII] and UV emission (see Fujimoto et al. 2020). Also, to be consistent with the other data points, the results by Herrera-Camus

dwarf sources. Our measurements provide a [CII]-to-UV size ratio ~ 1.2 , that is lower than the average ratio from high- z sources, and in much better agreement with the results by Herrera-Camus et al. (2021). The average [CII] size we obtain is consistent with that from high- z galaxies, possibly suggesting a common mechanism at the origin of the extended emission. In this regard, low-metallicity dwarf galaxies as those analyzed in this work are being considered analogs of high- z sources, sharing similar properties in terms of size, (sub-solar) metallicity, or specific SFR (e.g., Heckman et al. 2005; Motiño Flores et al. 2021; Shivaei et al. 2022). The UV emission, instead, results to be more extended for our local galaxies, in line with a possible $r_{e,UV}$ evolution with redshift (e.g., Shibuya et al. 2015, although this is disfavoured by the large UV size measured by Herrera-Camus et al. 2021). As suggested by Fudamoto et al. (2022), such a differential evolution between [CII] and UV sizes could imply an increasingly large reservoir of gas as compared to star-formation activity in galaxies at higher redshift.

4.3. Origin of the extended [CII] and FIR emission

Following Fujimoto et al. (2019, 2020), the formation of the extended [CII] emission around high- z galaxies could be explained by different processes, including satellite sources, large-scale photodissociation (and HII) regions, cold streams, galactic outflows, and tidal stripping. Although all of these phenomena could be responsible for the origin of [CII] halos, both observations and simulations agree on the fundamental role of outflows in the CGM enrichment.

Pizzati et al. (2020) made use of semi-analytical models to simulate the [CII] emission arising from supernova-driven cooling outflows, being successful in reproducing the ~ 10 kpc [CII] halos observed by Fujimoto et al. (2019) in $z \sim 6$ SFGs. Additionally, by combining cosmological hydrodynamic simulations and radiative transfer calculations, Arata et al. (2020) obtained extended [CII] radial profiles produced by star-formation-driven outflows that also partially matched Fujimoto et al. (2019) data. These theoretical works are supported by observations of cool outflows in the broad wings of [CII] line spectra, in conjunction with evidence for extended carbon emission in the same galaxies (Ginolfi et al. 2020b; Herrera-Camus et al. 2021). For instance, Ginolfi et al. (2020b) found outflow signatures in the stacked [CII] spectrum of $z \sim 5$ SFGs from ALPINE. When stacking sources with high SFR, they obtained much more spatially extended [CII] emission with respect to the case of lower-SFR galaxies, highlighting the star-formation-driven nature of the outflow. This could explain the positive correlation between $r_{e,[CII]}/r_{e,UV}$ and the stellar mass (thus SFR) found by Fujimoto

et al. (2021) were obtained by fitting the [CII], FIR and UV radial profiles with a Sérsic function instead of their adopted exponential one.

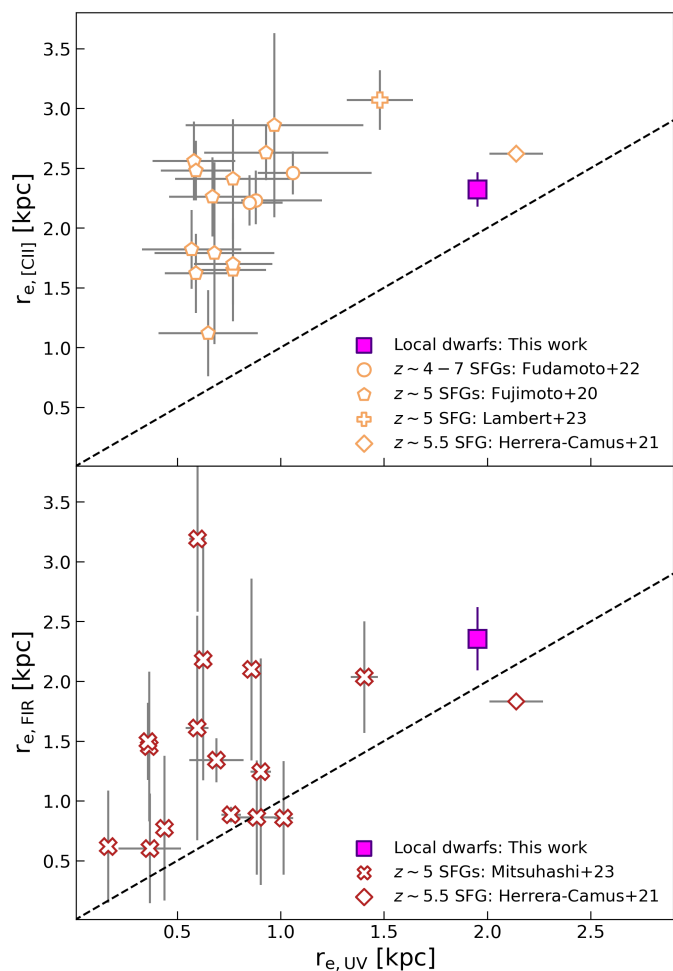


Fig. 2. Comparison between the UV, [CII] and FIR sizes. Empty markers represent [CII] (orange edge) and dust (red edge) measurements for $z \gtrsim 4$ SFGs from the literature (see Sect. 4.2 and 4.3). The magenta squares show the results for local dwarf galaxies from this work. The dashed black lines mark the 1:1 relation.

et al. (2020), ultimately suggesting that the physical origin of [CII] halos is linked to galactic outflows. Similarly, in Romano et al. (2023) we found that most of the individual local dwarf galaxies hosting prominent galactic outflows have the largest stellar masses and SFRs. Outflow velocities in those galaxies are larger than (or comparable with) the velocities needed by gas and dust to escape their dark matter halos, yielding to $\sim 40\%$ of the material entrained in the winds to be expelled in the IGM (and possibly an even larger fraction enriching the CGM). We consider all of this information as an evidence for stellar feedback producing the extended [CII] emission observed in Fig. 1.

On top of that, we note that the FIR continuum is as extended as the [CII] emission. This is in contrast with some observational and theoretical works on $z > 4$ SFGs usually finding that the cold dust is more compact than [CII] and UV continuum (e.g., Fujimoto et al. 2019, 2020; Ginolfi et al. 2020b; Herrera-Camus et al. 2021; Popping et al. 2022). However, a few examples of extended dust emission exist at high redshift. Fujimoto et al. (2020) identified one “Dust halo” object in their sample of ALPINE galaxies, with a FIR continuum profile similar to the [CII] one. Akins et al. (2022) characterized the morphological properties of a strongly-lensed galaxy at $z \sim 7$, observing an extended dust structure up to ~ 12 kpc, following the [CII] emis-

sion. Recently, Mitsuhashi et al. (2023) investigated the spatial extent of dust emission in $z \sim 5$ SFGs as part of the CRISTAL survey (2021.1.00280.L; PI: R. Herrera-Camus), which targeted a sub-sample of the ALPINE sources at higher resolution. They found that the dust continuum can extend up to several kpc, with the average effective radius in agreement with the typical [CII] size of galaxies at that redshift (i.e., ~ 2 kpc; Fujimoto et al. 2020), and ~ 2 times more extended than the rest-frame UV (at odds with expectations from current cosmological simulations; e.g., Popping et al. 2022). Such findings are also in agreement with our results from the local Universe (see Fig. 2, lower panel). This widespread dust in the CGM could be entrained by galactic outflows or tidal stripping of past merging events (e.g., McCormick et al. 2018; Triani et al. 2020; Kannan et al. 2021). There, it can rapidly become cold and hard to detect at high redshift due to the low sensitivity and the presence of the warmer cosmic microwave background (CMB; e.g., Vallini et al. 2015; Lagache et al. 2018), although correction factors for the CMB can alleviate that issue (e.g., da Cunha et al. 2013).

In the local Universe, we can reach much deeper sensitivity and the CMB temperature is low, not affecting the cold dust emission. The stacked FIR profile of our nearby dwarf sources extends to large radii, where dust could have been likely carried by galactic outflows in the past. This is in line with the results by McCormick et al. (2018), who made use of *Herschel* observations to detect cold dust in the CGM of six local dwarf galaxies affected by outflows. They found that dust can extend well beyond the stellar component, with a typical fraction of 10 – 20% of the total dust mass residing in the CGM. This fraction increases to $\sim 60\%$ for the galaxy with the largest metallicity deficit (obtained as the difference between the measured metallicity and the one predicted by mass-metallicity relation; Tremonti et al. 2004) in their sample, and with the largest evidence for dust entrained by galactic wind. If the evolution of primordial galaxies is ruled by similar processes as those observed in present-day low-metallicity dwarf sources, we could expect that extended dust components are generally present in the CGM of early SFGs, but too faint to be currently detected. In this scenario, the dust mass of high- z galaxies could be larger than estimates not accounting for extended FIR continuum (e.g., Akins et al. 2022), having deep implications for dust production mechanisms at early times (e.g., Nanni et al. 2020; Witstok et al. 2023).

5. Summary and conclusions

We present the first comparison between the spatial emission of [CII] 158 μm , FIR, and NUV continuum for local, low-metallicity dwarf galaxies. We used the sample of dwarf sources in Romano et al. (2023), taking advantage of GALEX and *Herschel* observations to produce stacked intensity maps in each band. We then compared the average radial profiles of the gas, dust, and stellar activity in the galaxies, obtaining an estimate of their physical size. Our findings are summarized below:

- The [CII] and dust continuum emissions in our galaxies are more extended than the star-formation activity traced by the NUV, that seems to be more centrally concentrated instead. By fitting the radial profiles with double Sérsic functions, we obtained ~ 2.4 kpc radius for both FIR and [CII], and ~ 1.9 kpc for NUV, implying a gas (or dust) over stellar ratio of ~ 1.2 .
- We compared our measurements with those from $z > 4$ SFGs, most of which show diffuse [CII] emission extending up to 10 kpc. The [CII] size of our sources is consistent

with that of primordial galaxies, suggesting a common mechanism at the origin of the emission. On the other hand, the UV continuum appears to be larger, pointing to a differential evolution between gas and star-formation activity across cosmic time (e.g., [Fudamoto et al. 2022](#)).

- Both observations and simulations agree about the fundamental role of galactic outflows in producing the extended [CII] emission detected in high- z galaxies. We found that atomic outflows traced by [CII] broad components are ubiquitous in our sources ([Romano et al. 2023](#)). In addition, given the resolution and sensitivity we reach in the local Universe, and having excluded galaxies with disturbed morphology from our analysis, we can rule out any contribution from ongoing merging or satellite galaxies to the observed diffuse [CII] emission in our sample⁴. All in all, we can thus affirm that outflows are most likely responsible for the CGM carbon enrichment of local dwarf galaxies.
- As a further imprint of outflow activity in nearby dwarf galaxies, we found that the average dust continuum is as extended as the [CII] emission. Dust in the CGM can be indeed carried by outflows, as shown by [McCormick et al. \(2018\)](#). At high redshift, only a few galaxies show similar, extended dust profiles (e.g., [Fujimoto et al. 2020](#); [Akins et al. 2022](#); [Mitsuhashi et al. 2023](#)), likely because, in general, it is hard to detect cold and faint CGM dust due to sensitivity limits and the CMB effect.

Our results highlight the importance of galactic outflows in the evolution of nearby low-mass galaxies and their primordial counterparts, as well as their imprint on the gas and dust distribution up to kiloparsec scales. Additionally, they could help calibrating ongoing [CII] intensity mapping experiments aimed at detecting the faintest SFGs in the Epoch of Reionization, so to understand their contribution to ionizing photons production and, more in general, to galaxy evolution in the early Universe (e.g., [Anderson et al. 2022](#); [Zhang et al. 2023](#)). Observations of individual galaxies at deeper sensitivity (e.g., with the new generation of single-dish telescopes like AtLAST) will allow us to ultimately disentangle the contribution of different mechanisms (e.g., outflows, minor mergers) to the observed diffuse gas and dust emission in these galaxies.

Acknowledgements. We thank the anonymous referee for her/his helpful comments and suggestions that improved the quality of our paper. This research made use of Photutils, an Astropy package for detection and photometry of astronomical sources ([Bradley et al. 2023](#)). This research made use of PetroFit ([Geda et al. 2022](#)), a package based on Photutils, for calculating Petrosian properties and fitting galaxy light profiles. M.R., A.N., and P.S. acknowledge support from the Narodowe Centrum Nauki (UMO-2020/38/E/ST9/00077). M.R. acknowledges support from the Foundation for Polish Science (FNP) under the program START 063.2023. G.C.J. acknowledges funding from ERC Advanced Grant 789056 “FirstGalaxies” under the European Union’s Horizon 2020 research and innovation programme. J. is grateful for the support from the Polish National Science Centre via grant UMO-2018/30/E/ST9/00082. D.D. acknowledges support from the National Science Center (NCN) grant SONATA (UMO-2020/39/D/ST9/00720).

References

Akins, H. B., Fujimoto, S., Finlator, K., et al. 2022, *ApJ*, 934, 64
Anderson, C. J., Switzer, E. R., & Bressye, P. C. 2022, *MNRAS*, 514, 1169

⁴ It is worth specifying that mergers and/or satellites can still be responsible for the extended [CII] reservoirs in galaxies’ CGM, especially in the high- z Universe, where interacting systems are more frequent (e.g., [Duncan et al. 2019](#); [Romano et al. 2021](#)) and observations are hampered by the worst angular resolution and sensitivity.

Arata, S., Yajima, H., Nagamine, K., Abe, M., & Khochfar, S. 2020, *MNRAS*, 498, 5541
Barbary, K. 2016, *Journal of Open Source Software*, 1, 58
Bertin, E. & Arnouts, S. 1996, *A&AS*, 117, 393
B  thermin, M., Fudamoto, Y., Ginolfi, M., et al. 2020, *A&A*, 643, A2
Bouwens, R. J., Smit, R., Schouws, S., et al. 2022, *ApJ*, 931, 160
Bradley, L., Sip  cz, B., Robitaille, T., et al. 2023, *astropy/photutils: 1.8.0*
Cicone, C., Maiolino, R., Gallerani, S., et al. 2015, *A&A*, 574, A14
Cormier, D., Abel, N. P., Hony, S., et al. 2019, *A&A*, 626, A23
da Cunha, E., Groves, B., Walter, F., et al. 2013, *ApJ*, 766, 13
D  az-Santos, T., Armus, L., Charmandaris, V., et al. 2017, *ApJ*, 846, 32
Duncan, K., Conselice, C. J., Mundy, C., et al. 2019, *ApJ*, 876, 110
Faisst, A. L., Schaerer, D., Lemaux, B. C., et al. 2020, *ApJS*, 247, 61
Fudamoto, Y., Smit, R., Bowler, R. A. A., et al. 2022, *ApJ*, 934, 144
Fujimoto, S., Ouchi, M., Ferrara, A., et al. 2019, *ApJ*, 887, 107
Fujimoto, S., Silverman, J. D., B  thermin, M., et al. 2020, *ApJ*, 900, 1
Gallerani, S., Pallottini, A., Feruglio, C., et al. 2018, *MNRAS*, 473, 1909
Geda, R., Crawford, S. M., Hunt, L., et al. 2022, *AJ*, 163, 202
Ginolfi, M., Jones, G. C., B  thermin, M., et al. 2020a, *A&A*, 643, A7
Ginolfi, M., Jones, G. C., B  thermin, M., et al. 2020b, *A&A*, 633, A90
Griffin, M. J., Abergel, A., Abreu, A., et al. 2010, *A&A*, 518, L3
Guo, Y., Maiolino, R., Jiang, L., et al. 2020, *ApJ*, 898, 26
Heckman, T. M., Hoopes, C. G., Seibert, M., et al. 2005, *ApJ*, 619, L35
Heintz, K. E., Watson, D., Oesch, P. A., Narayanan, D., & Madden, S. C. 2021, *ApJ*, 922, 147
Herrera-Camus, R., F  rster Schreiber, N., Genzel, R., et al. 2021, *A&A*, 649, A31
Hopkins, P. F., Quataert, E., & Murray, N. 2012, *MNRAS*, 421, 3522
Janjamasimanana, R., Koribalski, B. S., J  zsa, G. I. G., et al. 2022, *MNRAS*, 513, 2019
Jones, G. C., Maiolino, R., Circosta, C., et al. 2023, *MNRAS*, 518, 691
Jones, G. C., Vergani, D., Romano, M., et al. 2021, *MNRAS*, 507, 3540
Jonsson, P., Groves, B. A., & Cox, T. J. 2010, *MNRAS*, 403, 17
Kannan, R., Vogelsberger, M., Marinacci, F., et al. 2021, *MNRAS*, 503, 336
Lagache, G., Cousin, M., & Chatzikos, M. 2018, *A&A*, 609, A130
Lambert, T. S., Posses, A., Aravena, M., et al. 2023, *MNRAS*, 518, 3183
Le F  vre, O., B  thermin, M., Faisst, A., et al. 2020, *A&A*, 643, A1
Madden, S. C., Geis, N., Genzel, R., et al. 1993, *ApJ*, 407, 579
Madden, S. C., R  my-Ruyer, A., Galametz, M., et al. 2013, *PASP*, 125, 600
Madden, S. C., R  my-Ruyer, A., Galametz, M., et al. 2014, *PASP*, 126, 1079
Martin, D. C., Fanson, J., Schiminovich, D., et al. 2005, *ApJ*, 619, L1
McCormick, A., Veilleux, S., Mel  ndez, M., et al. 2018, *MNRAS*, 477, 699
McMullin, J. P., Waters, B., Schiebel, D., Young, W., & Golap, K. 2007, in *Astronomical Society of the Pacific Conference Series*, Vol. 376, *Astronomical Data Analysis Software and Systems XVI*, ed. R. A. Shaw, F. Hill, & D. J. Bell, 127
Mitsuhashi, I., Tadaki, K.-i., Ikeda, R., et al. 2023, *arXiv e-prints*, arXiv:2311.17671
Moti  o Flores, S. M., Wiklind, T., & Eufrazio, R. T. 2021, *ApJ*, 921, 130
Nanni, A., Burgarella, D., Theul  , P., C  t  , B., & Hirashita, H. 2020, *A&A*, 641, A168
P  roux, C. & Howk, J. C. 2020, *ARA&A*, 58, 363
Pineda, J. L., Langer, W. D., Velusamy, T., & Goldsmith, P. F. 2013, *A&A*, 554, A103
Pizzati, E., Ferrara, A., Pallottini, A., et al. 2020, *MNRAS*, 495, 160
Poglitich, A., Waelkens, C., Geis, N., et al. 2010, *A&A*, 518, L2
Popping, G., Pillepich, A., Calistro Rivera, G., et al. 2022, *MNRAS*, 510, 3321
Romano, M., Cassata, P., Morselli, L., et al. 2021, *A&A*, 653, A111
Romano, M., Nanni, A., Donevski, D., et al. 2023, *A&A*, 677, A44
Romanowsky, A. J. & Fall, S. M. 2012, *ApJS*, 203, 17
Rupke, D. S. N., G  ltekin, K., & Veilleux, S. 2017, *ApJ*, 850, 40
Sanderson, K. N., Prescott, M. K. M., Christensen, L., Fynbo, J., & M  ller, P. 2021, *ApJ*, 923, 252
S  rsic, J. L. 1963, *Bolet  n de la Asociaci  n Argentina de Astronom  a La Plata Argentina*, 6, 41
Shao, J. & Wu, C. F. J. 1989, *The Annals of Statistics*, 17, 1176
Shibuya, T., Ouchi, M., & Harikane, Y. 2015, *ApJS*, 219, 15
Shivaei, I., Popping, G., Rieke, G., et al. 2022, *ApJ*, 928, 68
Tremonti, C. A., Heckman, T. M., Kauffmann, G., et al. 2004, *ApJ*, 613, 898
Triani, D. P., Sinha, M., Croton, D. J., Pacifici, C., & Dwek, E. 2020, *MNRAS*, 493, 2490
Tumlinson, J., Peebles, M. S., & Werk, J. K. 2017, *ARA&A*, 55, 389
Vallini, L., Gallerani, S., Ferrara, A., Pallottini, A., & Yue, B. 2015, *ApJ*, 813, 36
Veilleux, S., Mel  ndez, M., Stone, M., et al. 2021, *MNRAS*, 508, 4902
Werk, J. K., Prochaska, J. X., Cantalupo, S., et al. 2016, *ApJ*, 833, 54
Witstok, J., Jones, G. C., Maiolino, R., Smit, R., & Schneider, R. 2023, *MNRAS*, 523, 3119
Zanella, A., Daddi, E., Magdis, G., et al. 2018, *MNRAS*, 481, 1976
Zhang, M., Ferrara, A., & Yue, B. 2023, *MNRAS*, 526, 4388

Appendix A: Stacked galaxies

We list in Table A.1 the dwarf galaxies from Romano et al. (2023), indicating which targets have been used in the NUV, FIR and [CII] stacking. We also show in Fig. A.1 some physical parameters of the sources in the final stacked samples, as obtained in Romano et al. (2023). Although our three samples of galaxies have different number of sources, they share similar properties in terms of redshift, stellar mass, and SFR. This reassures us that a comparison between the average radial profiles of the stacked samples is still very informative.

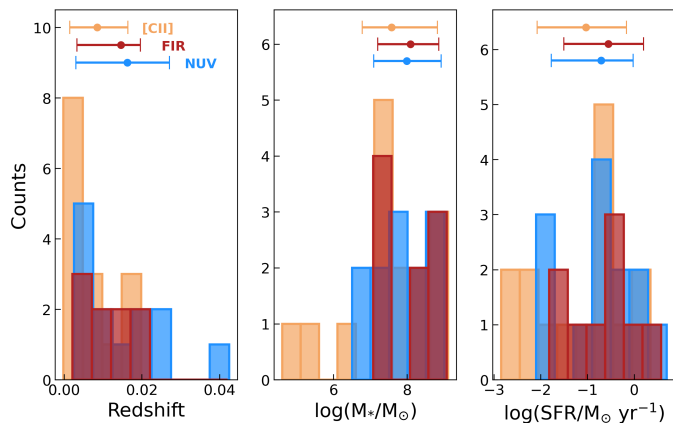


Fig. A.1. Redshift, stellar mass, and SFR distributions (from left to right) for our samples of galaxies with [CII], FIR, and NUV emission (orange, red, and lightblue histograms, respectively). Circles with error bars (obtained from the 16th and 84th percentiles of each distribution) indicate the average and corresponding uncertainty of the samples.

Galaxy inclination. In principle, galaxies’ orientation could have a significant effect on the stacking results. If galaxies are randomly oriented in the sky, stacking will tend to average over different inclination angles. In case of preferred orientation towards edge-on sources instead, the gas and dust distribution could be biased (e.g., Jonsson et al. 2010). To check for this, we estimated the inclination angles of our galaxies as $i = \arccos(b/a)$, where b and a are the corresponding minor and major axis from Madden et al. (2013). The resulting distribution of inclinations has an average of ~ 36 deg, which points towards face-on galaxies (i.e., $i = 0$), and that is smaller than the average inclination of 60 deg expected from randomly oriented sources in the sky (e.g., Romanowsky & Fall 2012). Only three galaxies (namely, IIZw40, SBS1415, UGC4483) have inclinations larger than 56 deg (i.e., the 84th percentile of the distribution), thus representing possible outliers in the stacking. However, by removing these sources from the stacking, we found effective radii in agreement within 1σ with those obtained from the full samples. Therefore, we can exclude any significant impact of galaxies’ inclination on our results.

Appendix B: Radial profiles fitting

We show here the comparison between the fit of the NUV, [CII], and FIR radial profiles when assuming a single or double Sérsic function, as introduced in Sect. 4.

Figure B.1 displays the radial profiles extracted as explained in Sect. 3.4, along with the residuals obtained with a single (dotted lines) and double (solid lines) Sérsic fitting. As evident from the residuals, the latter is in much better agreement with the data

Table A.1. Sample of dwarf galaxies from Romano et al. (2023).

Source name	NUV	FIR	[CII]
Haro2	✓	-	✓
Haro3 (*)	-	-	-
Haro11	✓	✓	-
He2-10	-	-	✓
HS0052+2536	✓	✓	-
HS1222+3741	✓	-	✓
HS1304+3529	-	✓	✓
HS1330+3651	-	✓	✓
HS1442+4250	-	-	-
HS2352+2733	✓	-	-
IZw18	✓	-	✓
IIZw40	✓	-	✓
Mrk153	✓	✓	✓
Mrk209	-	-	✓
Mrk930	✓	✓	✓
Mrk1089 (*)	-	-	-
Mrk1450	-	✓	✓
SBS0335-052	✓	-	-
SBS1159+545	-	-	-
SBS1211+540	✓	-	-
SBS1249+493	✓	-	-
SBS1415+437	-	✓	✓
SBS1533+574	✓	✓	✓
UGC4483	-	-	✓
UM133	-	-	✓
UM311	-	-	-
UM448 (*)	-	-	-
UM461	✓	✓	-
VIIZw403	-	-	✓

Notes. Check marks indicate whether the NUV, FIR, and [CII] maps of the corresponding galaxy have been used in the stacking. Sources with (*) represent galaxies classified as mergers in Romano et al. (2023), and that have been excluded from the analysis.

with respect to the single Sérsic, suggesting that a diffuse component is needed to reproduce the profiles. It is worth noting that such extended component is more important for the dust continuum and [CII] line than for the stellar activity traced by the NUV emission.

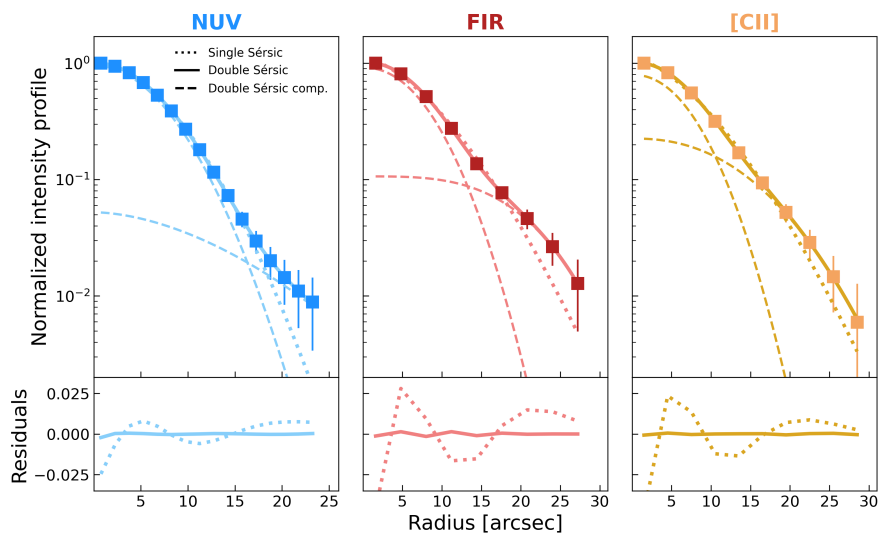


Fig. B.1. *Top panels:* Normalized intensity profiles for the convolved NUV continuum, FIR dust emission, and [CII] line (from left to right), as represented by the lightblue, red, and orange squares, respectively. In each panel, we show the best fit with a single (dotted line) and a double (solid line) Sérsic function. In this latter case, we also display the central and extended components of the fit with dashed lines. *Bottom panels:* Residuals of the fit to the corresponding profile with the single (dotted line) and double (solid line) Sérsic function.